Supporting Information

Supporting Information Corrected March 18, 2019
Xu et al. 10.1073/pnas.1717022115

Linear Model for Undulatory Wave Propagation

We first developed a linear coupling model to simulate wave propagation along the body of *C. elegans*. In this model, the head motor circuit contains an oscillator that dominates the rhythmic motion of the whole body (1). Other segments cannot oscillate by themselves but oscillate according to the proprioceptive input from the anterior segment. This simple phenomenological model does not simulate the detailed dynamics of individual neurons but instead aims to elucidate several key properties of wave propagation based on a linear model.

The worm head motor circuit consists of a different group of motor neurons. Indeed, when all B-type motor neurons were optogenetically ablated, head rhythmic activity persisted during forward locomotion. Because neural mechanisms for generating head bending activity remain largely elusive, we, for simplicity, imposed sinusoidal head bending curvature for k_1 at defined temporal frequency. Apart from the head, we divided the worm body into five segments (the number of segments was not essential for our theoretical argument), each with different dynamics, as described in Eq. **1**. Eq. **1** also arises naturally from a biologically more realistic model, where dorsal and ventral activities are treated separately. In this case, we have the following:

$$\begin{cases} C_m\dfrac{dv_{di}}{dt}=g_m(-v_{di}+ck_{i-1})-g(v_{di}-v_{AVB}) \\ \tau_h\dfrac{du_{di}}{dt}=-u_{di}+v_{di} \\ C_m\dfrac{dv_{vi}}{dt}=g_m(-v_{vi}-ck_{i-1})-g(v_{vi}-v_{AVB}) \\ \tau_h\dfrac{du_{vi}}{dt}=-u_{vi}+v_{vi} \\ \tau_\eta\dfrac{dk_i}{dt}=-k_i+\alpha_{\max}*(u_{di}-u_{vi})/b \end{cases} \quad \text{body,} \quad i=2,3,\ldots. \qquad \textbf{[S1]}$$

Subscripts d and v denote dorsal and ventral sides, respectively. If we subtract "dorsal" equations from "ventral" equations, Eq. **1** will be derived, provided we consider that dorsal and ventral motor activities are antiphased, namely $v_d=-v_i$ and $v_{di}=-v_{vi}$. Simulation using Eq. **S1** did not show any essential difference compared with simulation using Eq. **1**.

We set AVB membrane potential at a constant depolarized value in our model because AVB has gap junction coupling with all B-type motor neurons. During forward locomotion, B-type neurons are at distinct oscillatory phase: some are depolarized and some are hyperpolarized. The net electrical currents AVB received are canceled out and remain roughly constant. This assumption is consistent with calcium imaging data of AVB, which exhibited elevated yet nonoscillatory activity during forward locomotion.

The linear model makes two predictions that can be tested experimentally. First, abolishing head motor activity should eliminate undulatory wave propagation. However, when the head and body were decoupled in our experiments, we observed high-frequency oscillation emerging from the midbody. Second, while simulation suggested AVB-B gap junction coupling would deteriorate the propagation of the bending amplitude (Fig. 2*D*), our experimental data revealed the opposite. This result was independent of the value of v_{AVB}.

Parameters used in simulation are as follows:

$$\alpha_{\max}/b=2\ \text{mm}^{-1},$$

$$C_m=4.5\ \text{pF},\ g_m=100\ \text{pS},\ c=0.65\ \text{mm},\ \tau_h=75\ \text{ms},$$

$$\tau_\eta=\frac{C_N}{b}\left(\frac{\lambda}{2\pi}\right)^4\approx\frac{30\eta}{b}\left(\frac{\lambda}{2\pi}\right)^4,\ b=9.5\times10^{-14}\text{N*m}^2,\ \lambda=1\,\text{mm},$$

$$\eta=1\,\text{Pa*s}.$$

Analytical Solution to Linear Model

To gain a deeper insight into the bending amplitude decay during wave propagation (Fig. 2*D*), we developed an analytical understanding for the linear coupling model by considering the following continuous model:

$$\begin{cases} C_m\dfrac{\partial v}{\partial t}=g_m(-v+ck(x-l)) \\ \tau_\eta\dfrac{\partial k}{\partial t}=-k+\alpha_{\max}v/b \end{cases} \quad 0<x<L. \qquad \textbf{[S2]}$$

In the first equation, $ck(x-l)$ describes how proprioceptive couplings drive the change in neural activity in motor neurons. l is the characteristic length of proprioceptive coupling from an anterior body region, and L is the length of the worm. The second equation relates the change of body shape with neural activity. For simplicity, we dropped the equation that relates neural activity and muscle torque in Eq. **1**. The delay time between neural activity and muscle torque, characterized by τ_h, was absorbed by the time constant τ_η in Eq. **S2**. Because proprioceptive coupling is local, we impose $l\ll L$.

We assert a harmonic motion to describe the motor activity of the head. Thus, $v(x)$ and$k(x)$ can be written as follows:

$$\begin{cases} v=v_0\exp\left(i\left(\dfrac{2\pi x}{\lambda}-\omega t\right)\right) \\ k=k_0\exp\left(i\left(\dfrac{2\pi x}{\lambda}-\omega t\right)\right) \end{cases} \quad x\le 0. \qquad \textbf{[S3]}$$

The neural activity and curvature are not in-phase. Thus, the phase factors are absorbed into coefficients v_0 and k_0, which are all complex numbers.

The self-consistent solution for the motor activity along the body is sinusoidal, namely,

$$\begin{cases} v=V(x)\exp\left(i\left(\dfrac{2\pi x}{\lambda}-\omega t\right)\right) \\ k=K(x)\exp\left(i\left(\dfrac{2\pi x}{\lambda}-\omega t\right)\right) \end{cases} \quad 0<x<L. \qquad \textbf{[S4]}$$

Substituting Eq. **S4** into Eq. **S2** and defining $\tau_m=C_m/g_m$, we have the following:

$$-i\omega\tau_mV(x)=-V(x)+c\exp\left(-i\frac{2\pi l}{\lambda}\right)K(x-l), \qquad \textbf{[S5]}$$

$$-i\omega\tau_\eta K(x)=-K(x)+\alpha_{\max}V(x)/b. \qquad \textbf{[S6]}$$

Replacing $K(x-l)$ with $K(x)-K'(x)l+K''(x)l^2/2$, and using $l \ll \lambda$, we find the following:

$$\frac{cl^2}{2}K''(x)-clK'(x)+\left((i\omega\tau_m-1)\left(1-i\omega\tau_\eta\right)b/\alpha_{\max}+c\right)K(x)=0. \quad \textbf{[S7]}$$

The solution is as follows:

$$K(x)=k_0\exp\left(-\frac{B+\sqrt{B^2-4AC}}{2A}x\right), \quad \textbf{[S8]}$$

where

$$A=\frac{cl^2}{2}, \quad B=-cl, \quad C=(i\omega\tau_m-1)\left(1-i\omega\tau_\eta\right)b/\alpha_{\max}+c.$$

Thus, the decaying length constant satisfies the following:

$$1/\xi=\mathrm{Re}\frac{B+\sqrt{B^2-4AC}}{2A}. \quad \textbf{[S9]}$$

Expanding it to power series of ω and only preserving lower order terms, we have the following:

$$\xi=\frac{l}{1-\frac{c\alpha_{\max}}{b}+\omega^2\left(\frac{c\alpha_{\max}\left(\tau_m^2+\tau_\eta^2\right)}{2b}+\left(\frac{c\alpha_{\max}}{b}-1\right)\tau_m\tau_\eta\right)}. \quad \textbf{[S10]}$$

The time constant τ_η increases with viscosity of medium η, and the decay length constant ξ decreases with η.

To the leading order, the decay length constant can be approximated as follows:

$$\xi\approx\frac{l}{1-\frac{c\alpha_{\max}}{b}}. \quad \textbf{[S11]}$$

Note that Eq. **S11** is consistent with the discrete model with nearest neighbor coupling, at least to the leading order. In the discrete model of nearest-neighbor coupling, the curvatures follow the relationship $k_i\approx c\alpha_{\max}/bk_{i-1}$ (2). So the decaying rate should be $k_{i-1}-k_i/k_{i-1}l\approx(1-c\alpha_{\max}/b)/l$, which is identical to the result from the continuous model.

When we incorporate electrical couplings between AVB interneurons and B-type neurons into this model, the equations become the following:

$$\begin{cases}\tau_m\dfrac{\partial v}{\partial t}=-v-gv/g_m+ck(x-l)\\ \tau_\eta\dfrac{\partial k}{\partial t}=-k+\alpha_{\max}v/b\end{cases} \quad 0<x<L, \quad \textbf{[S12]}$$

where g is the gap junction conductance. In this case, the decay length constant, to the leading order, reduces to the following:

$$\xi\approx\frac{l}{1-\frac{g_mc\alpha_{\max}}{(g+g_m)b}}, \quad \textbf{[S13]}$$

which further deteriorates the propagation of the bending amplitude. Note that, although the effective τ_m is also smaller, $\tau_m\to\tau_m/(1+g/g_m)$, its contribution is mostly to the second order and does not change the conclusion. This prediction is inconsistent with our experimental observations.

Nonlinear Model

The discrepancy between our theoretical and experimental observations forced us to develop a modified nonlinear model. For the head oscillator, we still imposed dorsal–ventral anticorrelated bending activities at a defined temporal frequency. For all other segments, our model incorporated the experimental observations that B-type motor neurons generate oscillations when the head and body are decoupled and when AVB interneurons and B-type motor neurons are electrically coupled ($g>0$). The intrinsic membrane properties in the B-type motor neurons remain unknown. For simplicity, we developed a phenomenological model based on active Ca^{2+} and K^+ conductances (3).

The motor activity in a given body segment is now governed by the following equations:

$$\begin{cases}C_m\dfrac{dV_{di}}{dt}=-g_L(V_{di}-E_L)-g_{Ca}m_\infty(V_{di})*(V_{di}-E_{Ca})-g_Kn_{di}*(V_{di}-E_K)+c'k_{i-1}+g(V_{AVB}-V_{di})\\ \tau_n\dfrac{dn_{di}}{dt}=-n_{di}+n_\infty(V_{di})\\ C_m\dfrac{dV_{vi}}{dt}=-g_L(V_{vi}-E_L)-g_{Ca}m_\infty(V_{vi})*(V_{vi}-E_{Ca})-g_Kn_{vi}*(V_{vi}-E_K)-c'k_{i-1}+g(V_{AVB}-V_{vi})\\ \tau_n\dfrac{dn_{vi}}{dt}=-n_{vi}+n_\infty(V_{vi})\\ \tau_u\dfrac{dM_{di}}{dt}=-M_{di}+M(V_{di})-M(V_{vi})\\ \tau_u\dfrac{dM_{vi}}{dt}=-M_{vi}+M(V_{vi})-M(V_{di})\\ \tau_\eta\dfrac{dk_i}{dt}=-k_i+\alpha'_{max}/b*(M_{di}-M_{vi})\end{cases} \quad \textbf{[S14]}$$

In Eq. **S14**, m,n are voltage-dependent gating variables; $m_\infty(V)$, $n_\infty(V)$ are steady-state activation functions. We assume that the time constant for the gating variable m is small and m follows instantaneously with the voltage. $M(V)$ relates cell membrane potential and muscle torque. We assume they all have sigmoidal functional forms:

$$m_\infty(V)=\frac{1}{1+\exp\left(\frac{V-V_m}{\theta_m}\right)},\quad n_\infty(V)=\frac{1}{1+\exp\left(\frac{V-V_n}{\theta_n}\right)},\quad M(V)=\frac{1}{1+\exp\left(\frac{V-V_{mus}}{\theta_{mus}}\right)}. \qquad \textbf{[S15]}$$

$g(V_{AVB}-V)$ is the current flowing through the gap junction between AVB interneurons and B-type neurons, where V_{AVB} is the membrane potential of the AVB interneurons, held at a constant value.

The terms $-M(V_v)$ and $-M(V_d)$ in Eq. **S14** reflect contralateral inhibition from the D-type GABAergic motor neurons: dorsal D neurons can be activated by ventral B neurons and thereby inhibit dorsal muscle activity, and vice versa.

We simulated six segments (including the head), similar to that in the linear coupling model. The segment number was roughly in accordance with the number of DB-type motor neurons. The parameter values are listed below:

$$C_m=3.0\ \text{pF},\quad \tau_n=30\ \text{ms},\quad \tau_u=85\ \text{ms},$$

$$\tau_\eta=\frac{C_N}{b}\left(\frac{\lambda}{2\pi}\right)^4\approx\frac{30\eta}{b}\left(\frac{\lambda}{2\pi}\right)^4,$$
$$b=9.5\times10^{-14}\ \text{N}*\text{m}^2,\quad \lambda=1\,\text{mm},$$

$$g_L=100\ \text{pS},\quad g_{Ca}=400\,\text{pS},\quad g_K=500\ \text{pS},$$

$$c'=5*10^{-16}\ \text{A/m},\quad \alpha'_{\max}/b=2.1\ \text{mm}^{-1},$$

$$E_L=-60\ \text{mV},\quad E_{Ca}=60\ \text{mV},\quad E_K=-70\ \text{mV},\quad V_{AVB}=-20\ \text{mV},$$

$$V_m=-29\ \text{mV},\quad V_n=-55\ \text{mV},\quad V_{mus}=-45\ \text{mV},$$

$$\theta_m=10.25\ \text{mV},\quad \theta_n=20\ \text{mV},\quad \theta_{mus}=10\ \text{mV},$$

$$\eta=1\,\text{Pa}*\text{s}.$$

Comparing the case $g=0$ and $g=100\,\text{pS}$, we found that gap junction coupling between AVB interneurons and B-type neurons could equalize the bending amplitude (Fig. 5*C*). High-frequency oscillation within middle segments could also be generated when the head and body were decoupled (Fig. 5*A*).

1. Karbowski J, Schindelman G, Cronin CJ, Seah A, Sternberg PW (2008) Systems level circuit model of *C. elegans* undulatory locomotion: Mathematical modeling and molecular genetics. *J Comput Neurosci* 24:253–276.
2. Wen Q, et al. (2012) Proprioceptive coupling within motor neurons drives *C. elegans* forward locomotion. *Neuron* 76:750–761.
3. Izhikevich EM (2007) *Dynamical Systems in Neuroscience: The Geometry of Excitability and Bursting* (MIT Press, Cambridge, MA).

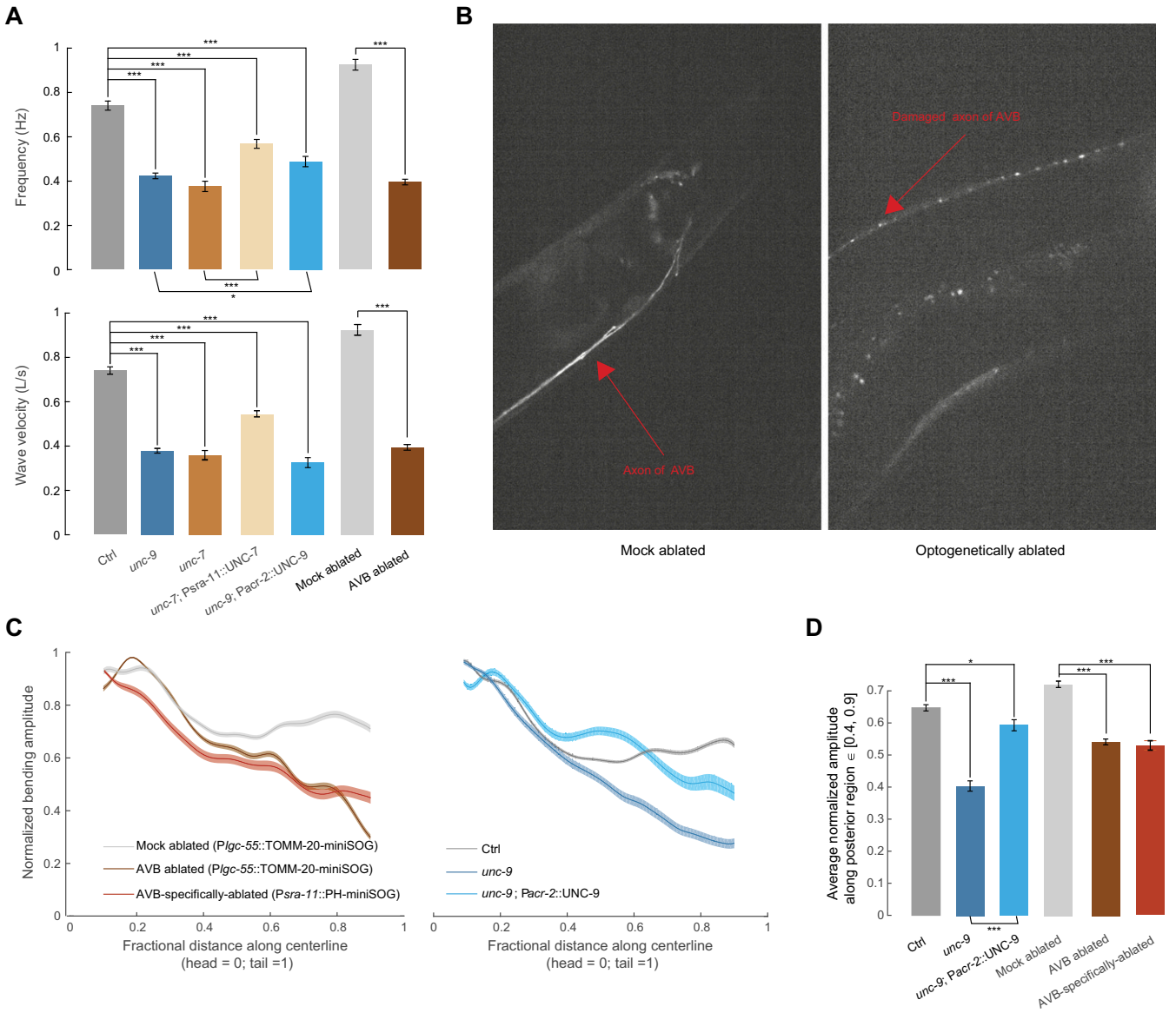

Fig. S1. AVB-B electrical couplings facilitate undulatory wave propagation during forward locomotion. (*A*) Locomotion kinematics of tested strains. *Upper* shows the comparison of undulation frequency in viscous medium (~1 Pa·s). *Lower* shows the comparison of wave velocity, calculated in worm body length per second (*L*/*s*). Error bars show SEM. ***$P < 0.0001$, *$P = 0.01$, two-sample *t* test with Bonferroni correction. Ctrl [N2; P*acr-5*::Arch; P*unc-4*::TWK-18(gf)], n = 107 measurements, 13 worms; *unc-7* mutant [*unc-7*(*hp121*); P*acr-5*::Arch; P*unc-4*::TWK-18(gf)], n = 99 measurements, 22 worms; *unc-9* mutant [*unc-9*(*fc16*); P*acr-5*::Arch; P*unc-4*::TWK-18(gf)], n = 144 measurements, 17 worms; AVB-ablated worms [P*glc-55*(B)::tom20::miniSOG::UrSL::wCherry], n = 80 measurements, 13 worms; Mock, n = 96 measurements, 12 worms. (*B*) Comparison of AVB axon fluorescence signals in mock and AVB-ablated worms. Arrows indicate intact and damaged axons. (*C*, *Left*) Comparison of normalized bending amplitude along the worm body in mock, AVB-ablated worms [P*lgc-55(B)*::tomm-20-miniSOG] and AVB-specifically ablated worms [P*sra-11*::PH-miniSOG]. (*C*, *Right*) Comparison of normalized bending amplitude along the worm body in CTRL, *unc-9*, and UNC-9 rescue in B-type and A-type motor neurons [*unc-9*(*fc16*); P*acr-2*::UNC-9; P*acr-5*::arch]. Rescue of UNC-9 in B-type and A-type motor neurons largely restored the posterior bending amplitude. Shaded regions show SEM. (*D*) Bending amplitude averaged over the posterior region ∈ [40, 90] of the worm body. ***$P < 0.0001$, *$P = 0.003$, two-sample *t* test with Bonferroni correction. Error bars represent SEM. Ctrl, n = 105 measurements, 13 worms; *unc-9* mutant, n = 93 measurements, 17 worms; UNC-9 rescue in motor neurons, n = 64 measurements, 9 worms. Mock-ablated ([P*lgc-55*::tomm-20-miniSOG] without ablation), n = 96 measurements, 12 worms; AVB-ablated [P*lgc-55(B)*::tomm-20-miniSOG], n = 80 measurements, 13 worms; AVB-specifically ablated [P*sra-11*::PH-miniSOG], n = 78 measurements, 10 worms.

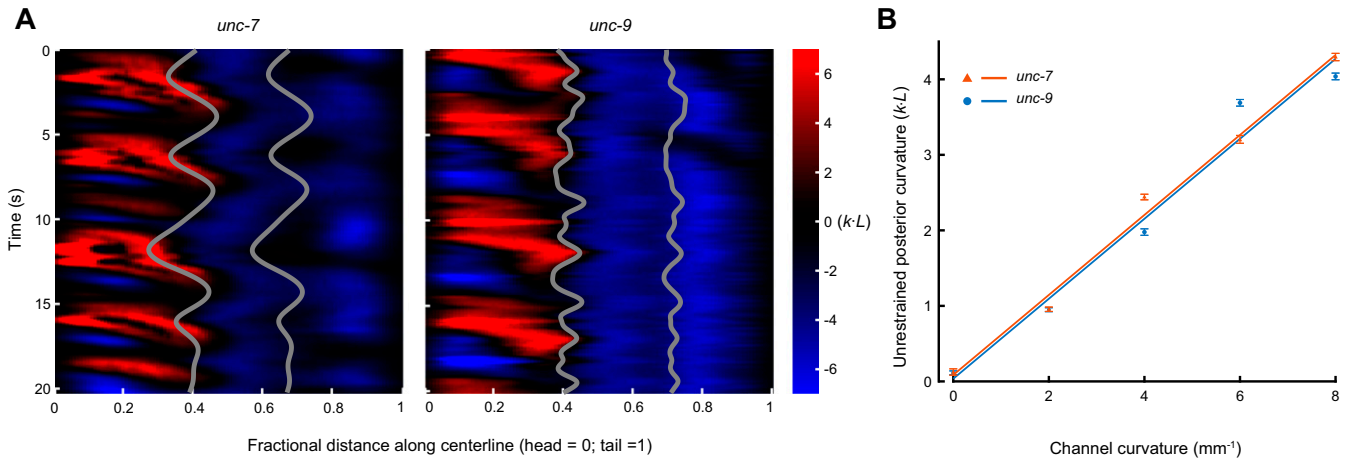

Fig. S2. AVB-B electrical couplings are not necessary for transducing proprioceptive signals. (*A*) Representative kymographs showing an *unc-7* mutant [*unc-7* (hp121); P*unc-4::*TWK-18(gf)] and an *unc-9* mutant worm [*unc-9*(fc16); P*unc-4::*TWK-18(gf)], whose midbodies were restrained in a microfluidic channel with defined curvature (6 mm^{-1}). Gray lines indicate anterior and posterior boundaries of the channel. (*B*) Unrestrained posterior body curvature as a function of channel curvature. Each data point: $n = 5$ worms; error bars represent SEM. Blue and red lines are linear fit ($R^2 > 0.97$).

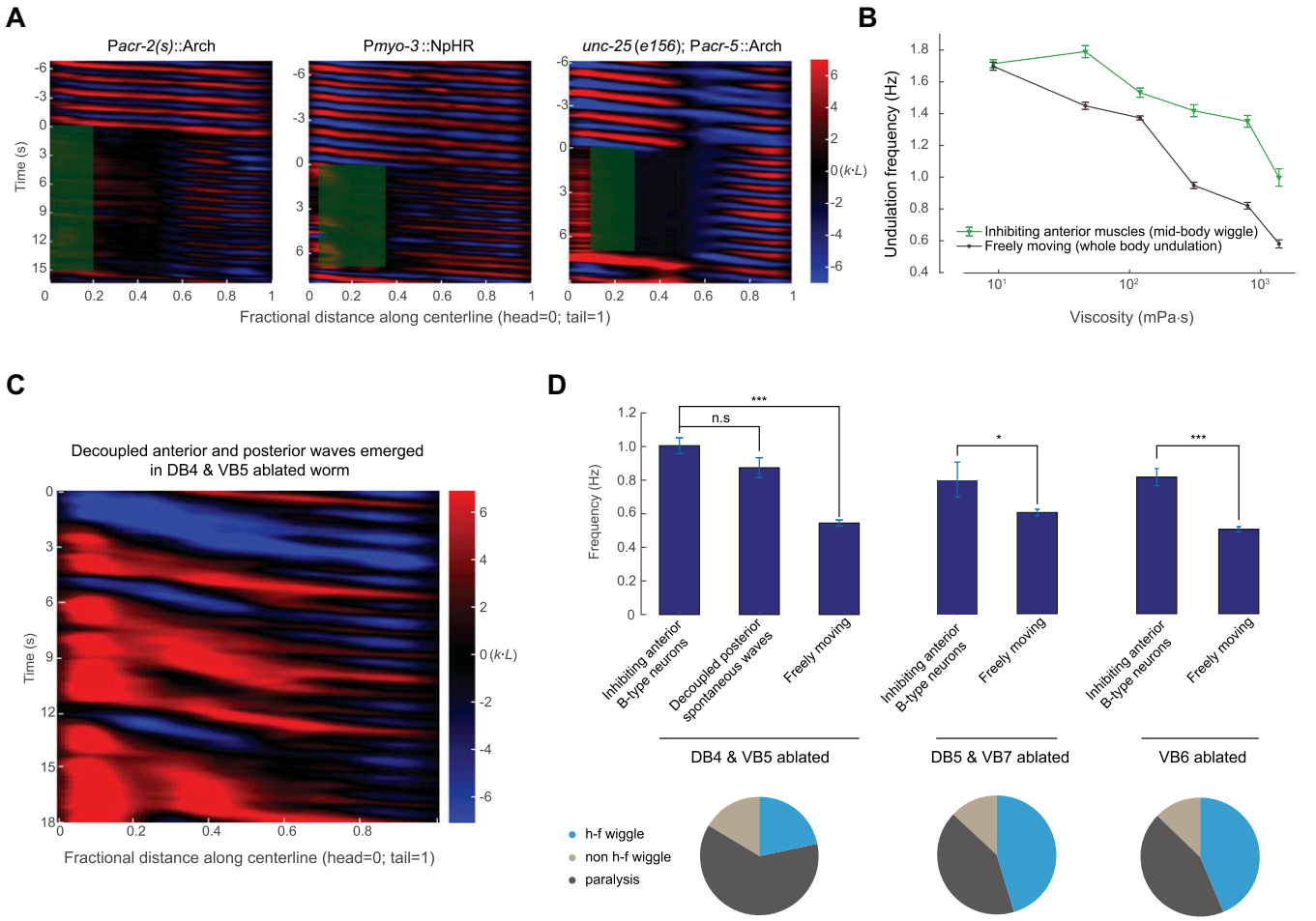

Fig. S3. Midbody B motor neurons generated rhythmic activity. (*A*) Representative kymographs demonstrate that fast mid/posterior body undulatory waves could be induced by inhibiting anterior A- and B-type motor neurons (P*acr-2*::Arch, 11 of 25 measurements) by inhibiting anterior muscle cells (P*myo-3*::NpHR, 52 of 87 measurements) or by inhibiting anterior B-type motor neurons in GABA neurotransmitter-deficient worms [*unc-25(e156)*; P*acr-5*::Arch, 33 of 45 measurements]. (*B*) Undulation frequency with medium viscosity. Black, normal swimming worm; green, midbody undulation when the head and body were decoupled by inhibiting anterior muscle cells. Each data point represents mean and SEM from $n \geq 4$ worms. (*C*) Representative kymographs of a freely swimming worm in which DB4 and VB5 motor neurons were optogenetically ablated (P*acr-5*::tomm20::miniSOG). Decoupled spontaneous waves emerged from anterior and posterior body regions. (*D*, *Top*) Summary of undulation frequencies after selectively ablating a subset of B-type motor neurons in the midbody. Three behavioral outcomes were compared. (*i*) Fast midbody undulation induced by optogenetically inhibiting anterior B-type motor neurons. (*ii*) Spontaneous posterior bending waves in DB4 and VB5-ablated worms. (*iii*) Freely swimming worms. (*Bottom*) Pie chart summarizes worm locomotor states across trials during optogenetic inhibition of anterior B-type motor neurons. State definitions can be found in the main text. Error bars show SEM. ***$P <$ 0.0001; *$P = 0.01$; n.s., $P = 0.15$, two-sample *t* test. DB4 and VB5 ablated $n = 11$ worms, DB5 and VB7 ablated $n = 8$ worms, VB6 ablated $n = 9$ worms.

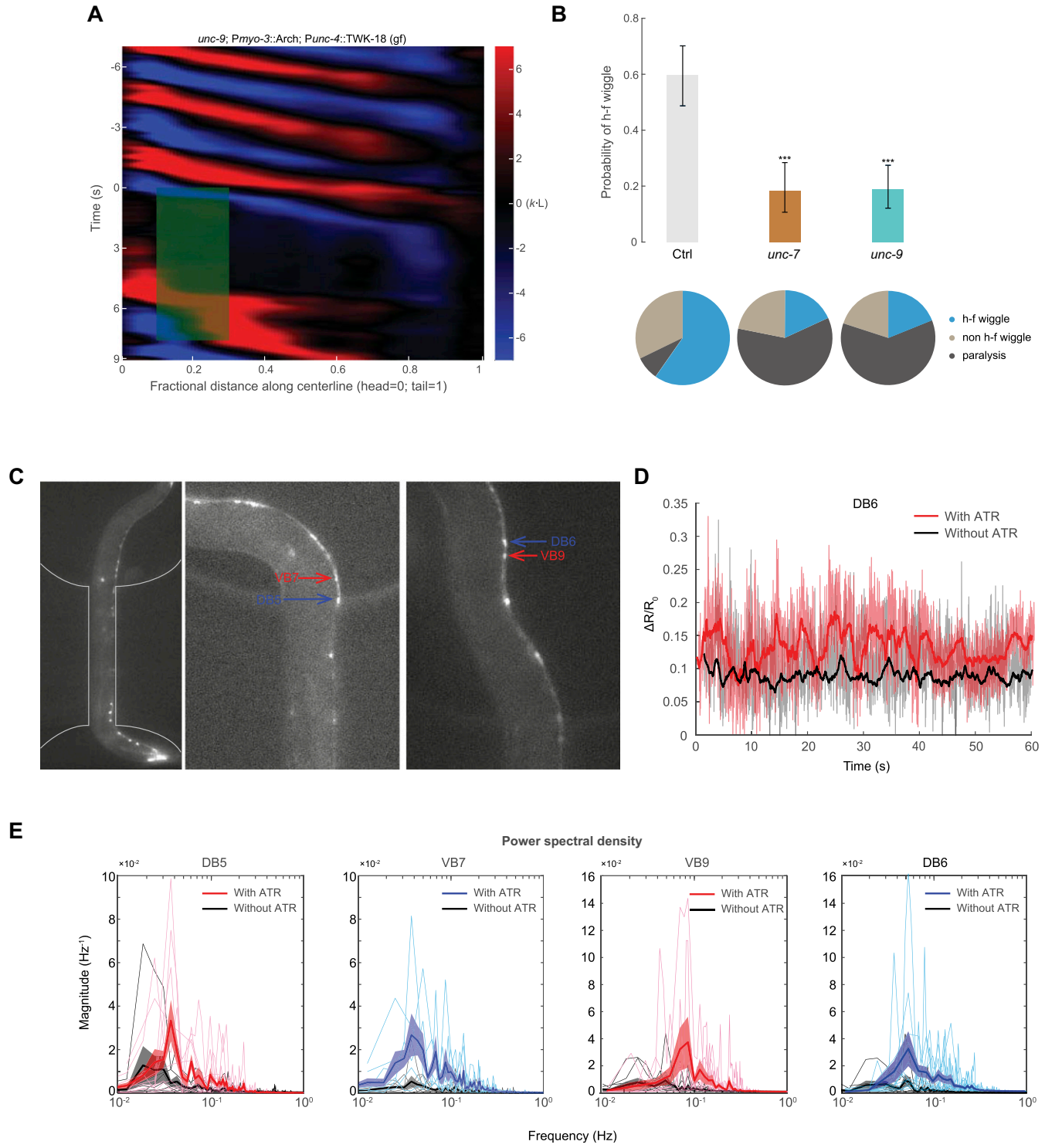

Fig. S4. AVB-B electrical couplings drive a bifurcation in B-type neuron dynamics. (*A*) Representative curvature kymographs of head-body–decoupled experiments in AVB-B gap junction-deficient *unc-9* mutants [*unc-9*; P*myo-3*::Arch; P*unc-4*::TWK-18(gf)]. Anterior muscle cells were optogenetically inhibited to abolish the proprioceptive signals arising from head bending activity. (*B*) Probability for inducing high-frequency midbody undulation when the head and body were decoupled by inhibiting anterior muscle cells. Pie chart summarizes worm locomotor states across trials. Error bars indicate 95% binomial proportion confidence interval. ***$P < 0.0001$, χ^2 test. Ctrl [P*myo*-3::NpHR, P*unc-4*::TWK-18(gf)], $n = 87$ measurements, 10 worms. *unc-7* mutant [*unc-7(hp121)*; P*myo*-3::Arch; P*unc-4*::TWK-18(gf)], $n = 82$ measurements, 18 worms. *unc-9* mutant [*unc-9(fc16)*; P*myo*-3::Arch; P*unc-4*::TWK-18(gf)], $n = 111$ measurements, 21 worms. (*C*) Video images of B-type motor neuron calcium imaging. To eliminate the proprioceptive coupling signal, we restrained the body region anterior to the imaging neurons within a straight microfluidic channel. (*D*) Raw and smoothed calcium dynamics of identified neurons when AVB interneurons were optogenetically activated (with ATR). Calcium imaging of worms without feeding ATR were used as control. (*E*) Power spectral density of smoothed B-type neuron calcium dynamics in the presence/absence of optogenetic activation of AVB interneurons. Darker plots were averaged density across worms ($n \geq 6$ worms in all cases); shaded regions are SEM.

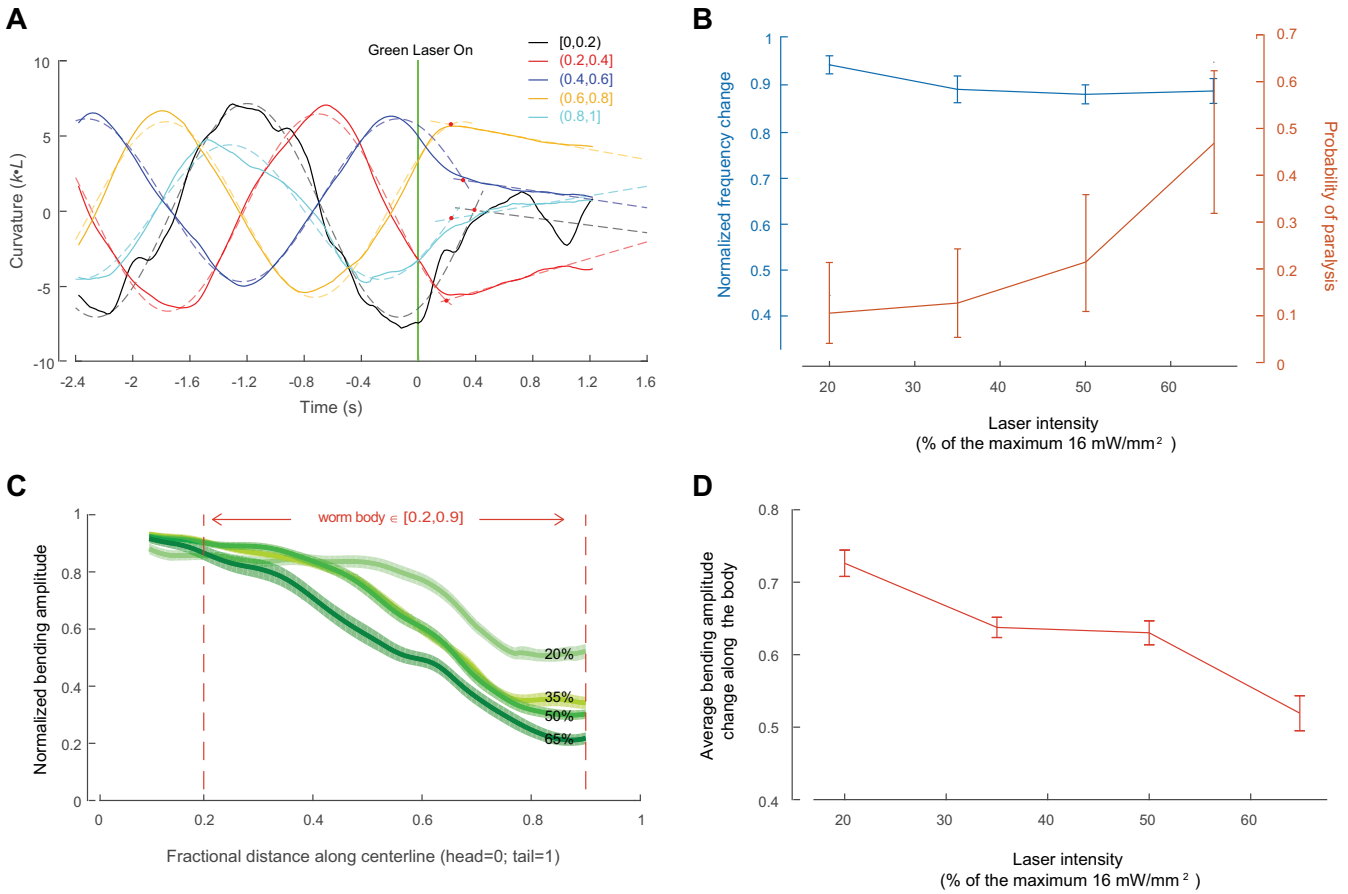

Fig. S5. Electrical couplings between motor neurons allow for rapid and reciprocal interactions between head and body motor activities. (*A*) Estimation of reaction time when midbody B-type motor neurons were optogenetically inhibited. First, we fit the regional curvature with a sinusoidal function right before the green laser was turned on. Second, we performed a linear fit of regional curvature during the optogenetic inhibition. The crossover point (red dot) represents the wiggle-to-paralysis transition for each segment. Curvatures were averaged over a defined color-coded region, represented by a fractional distance along the worm body coordinates (head = 0, tail = 1). (*B*) Dose-dependent effect on the undulation frequency and efficacy for inducing whole-body paralysis when B-type motor neurons within a posterior body region (∈ [0.7, 0.9]) were optogenetically inhibited. Error bars (blue), SEM; error bars (orange), 95% binomial proportion confidence interval. $n \geq 5$ worms for each data point. (*C*) Dose-dependent effect on the bending amplitude along the worm body when B-type motor neurons within a posterior body region (∈ [0.7, 0.9]) were optogenetically inhibited. Shaded regions are SEM. (*D*) Average bending amplitude change along the body ∈ [0.2, 0.9]. Error bars are SEM. Maximum laser intensity was 16 mW/mm^2.

Table S1. Strain information

Strain name	Experiment	Genotype	Construct (plasmid no.); injection concentrations for Ex lines
WEN0315	B motor neuron inhibition in WT	*wenIs0001*; *wenEx0315*	P*acr-5*::Arch::UrSL::wCherry (pJH2918); P*odr-1*::gfp (wenIs0001) P*unc-4*::TWK::18(gf)::UrSL::wCherry (pJH2108) 30 ng/μL; P*lin-14*::gfp 20 ng/μL; P*myo-3*::wCherry (pJH1774) 2.5 ng/μL (wenEx0315)
WEN0317	B motor neuron inhibition in *unc-7* mutants; microfluidic experiments	*wenIs0001*; *wenEx0317*; *unc-7*(*hp121*)	P*acr-5*::Arch:: UrSL::wCherry (pJH2918); P*odr-1*::gfp (WenIs0001) P*unc-4*::TWK::18(gf)::UrSL::wCherry (pJH2108) 30 ng/μL; P*lin-14*::gfp 20 ng/μL; P*myo-3*::wCherry (pjH1774) 2.5 ng/μL (wenEx0317)
WEN0304	B motor neuron inhibition in *unc-9* mutants; microfluidic experiments	*wenEx0304*; *hpEx2088*; *unc-9*(*fc16*)	P*acr-5*::Arch:: UrSL::wCherry (pJH2918) 30 ng/μL; P*lin-14*::gfp 20 ng/μL (Wen Ex0304) P*unc-4*::TWK::18(gf)::UrSL::wCherry (pJH2108); P*odr-1*::gfp (hpEx2088)
ZM7297	AVB ablation	*hpIs331*	P*lgc-55*(B)::tomm-20::miniSOG::UrSL::wCherry (pJH2890); lin-15
WEN0318	B motor neuron inhibition upon AVB ablation; microfluidic experiments	*wenIs0001*; *hpIs331*;	P*acr-5*::Arch::UrSL::wCherry (pJH2918); P*odr-1*::gfp (wenIs0001) P*lgc-55*(B)::tomm-20::miniSOG::UrSL::wCherry (pJH2890) (hpIs331)
WEN0335	B motor neuron inhibition in *unc-7* mutants, with UNC-7 restored in AVB	*wenEx0335*; *wenIs0001*; *unc-7*(*hp121*)	P*unc-4*::TWK::18(gf)::UrSL::wCherry (pJH2108) 30 ng/μL; P*sra-11*::UNC-7(cDNA)::wCherry (pJH2037) 20 ng/μL; P*lin-14*::gfp 20 ng/μL; P*myo-3*::wCherry 2.5 ng/μL (wenEx0335) P*acr-5*::Arch:: UrSL::wCherry (pJH2918); P*odr-1*::gfp (wenIs0001)
WEN0314	B motor neuron ablation; microfluidic experiments	*wenIs0001*; *hpIs374*;	P*acr-5*::Arch:: UrSL::wCherry (pJH2918); P*odr-1*::gfp (hpIs374) P*acr-5*::tomm-20::miniSOG::UrSL::wCherry (pJH2842) (wenIs0001)
WEN0001	B motor neuron inhibition	*wenIs0001*	P*acr-5*::Arch::UrSL::wCherry (pJH2918); P*odr-1*::gfp (wenIs0001)
WEN0320	B motor neuron inhibition upon AVB ablation	*wenIs0001*; *wenEx0320*	P*acr-5*::Arch::UrSL::wCherry (pJH2918); P*odr-1*::gfp (wenIs0001) P*sra-11*::tomm-20::miniSOG::UrSL::wCherry (quan0065) 50 ng/μL; P*myo-3*::wCherry 2.5 ng/μL (wenEx0320)
ZM9275	A and B motor neuron inhibition	*hpIs615*	P*acr-2*(s)::Arch::wCherry (pJH3717); Lin-15
ZX444.6	Muscle inhibition	*zxEx29*; *lin-15*(*n765ts*)	Pmyo-3::NpHR::ECFP; lin-15+ (zxEx29)
WEN0307	B motor neuron inhibition in *GABA*-deficient mutants	*wenIs0001*; *unc-25*(*e156*)	P*acr-5*::Arch::UrSL::wCherry (pJH2918); P*odr-1*::gfp (*wenIs0001*)
ZM7796	B motor neuron ablation	*hpIs374*	P*acr-5*::tomm-20::miniSOG::UrSL::wCherry (pJH2842)
ZM8424	B motor neuron Ca reporter	*hpIs458*	*Pacr-5*-GCaMP6s::wCherry (pJH3140); Lin-15
WEN0372	AVB activation	*wenEx*0372	P*sra-11*::Chrimson::wCherry (quan0164) 30 ng/μL; P*lin-14*::GFP (wenEx0372)
WEN0387	AVB inhibition	*wenEx0387*	P*sra-11*::GtACR2::wCherry (quan0235) 30 ng/μL; P*lin-14*::GFP (wenEX0387)
WEN0363	Muscle inhibition in *unc-7* mutants	*wenEx*0363; *unc-7*(*hp121*)	P*myo-3*::Arch::UrSL::wCherry (quan0124) 30 ng/μL; P*unc-4*::TWK-18(gf)::UrSL::wCherry (pJH2108) 30 ng/μL (wenEx0363)
WEN0323	Muscle inhibition in *unc-9* mutants	*wenEx0323*; *unc-9*(*fc16*)	P*myo-3*::Arch::UrSL::wCherry (quan0124) 30 ng/μL; P*unc-4*::TWK-18(gf)::UrSL::wCherry (pJH2108) 30 ng/μL (wenEx0323)
WEN0337	*unc-9* mutants with restored expression in A and B motor neurons	*wenEx0337*; *unc-9*(*fc16*)	P*acr-2*::UNC-9::wCherry (pJH1897) 2 ng/μL; P*acr-5*::Arch:: UrSL::wCherry (pJH2918) 30 ng/μL (wenEx0337)
WEN0366	Overexpression of UNC-9 in B motor neurons	*wenEx0366*	P*acr-5*::Arch:: UrSL::wCherry (pJH2918) 30 ng/μL; P*acr-5*::UNC-9 (pJH2140) 30 ng/μL (wenEx0366)
WEN0397	B motor neurons calcium imaging with AVB activation in *unc-13* mutants	*wenEx0393*; *hpIs458*; *unc-13(e51)*	P*sra-11*::Chrimson::wCherry (quan0164) 30 ng/μL; P*lin14*-GFP 20 ng/μL; (wenEX0393); P*acr-5*::GCaMP6::wCherry (*hpIs458*)
WEN0403	AVB interneurons specifically killing	*wenEx0403*	P*sra-11*::PH-miniSOG::SL2::wCherry (quan0253) 30 ng/μL; P*lin-14*::GFP (quan0051) 20 ng/μL

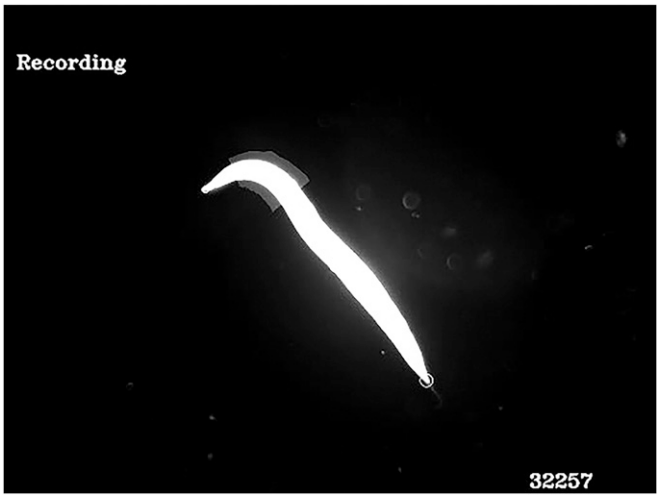

Movie S1. An *unc-7* mutant animal swam freely in solution at ~1 Pa·s viscosity. Despite anterior body undulation, the bending amplitude near the tail significantly diminished. Note that all movies were played at 0.5× speed.

Movie S1

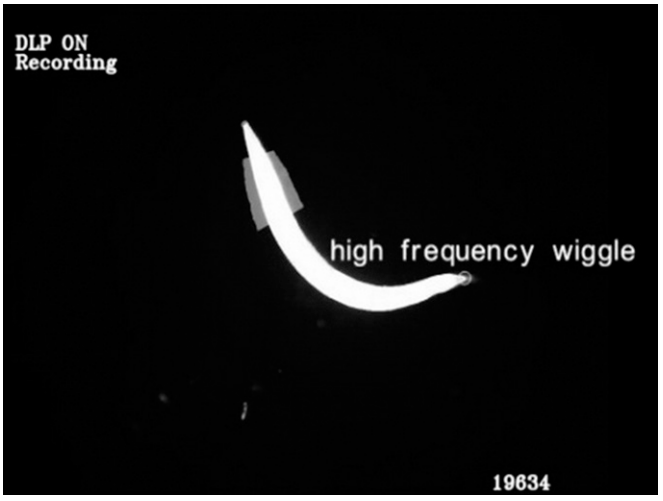

Movie S2. Optogenetic inhibition of the anterior region of a freely swimming wild-type worm induced high-frequency undulation in the posterior body region. Note that all movies were played at 0.5× speed.

Movie S2

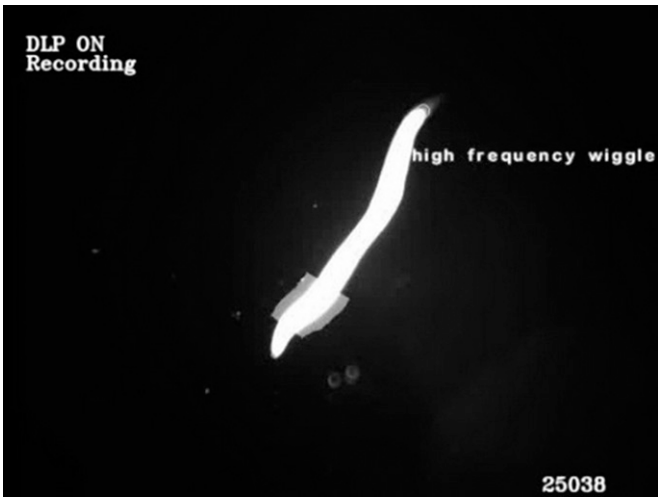

Movie S3. A worm with UNC-7 expression restored in AVB and other neurons (P*sra-11*::UNC-7) swam in solution at ~1 Pa·s viscosity. Both bending amplitude and high-frequency undulation in the posterior body region were restored. Note that all movies were played at 0.5× speed.

Movie S3

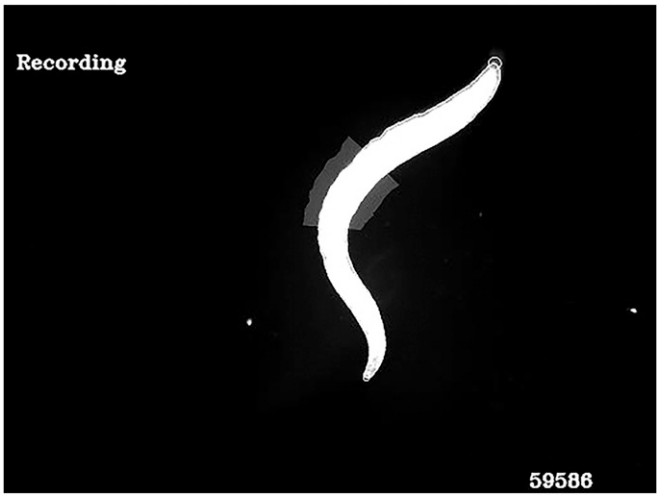

Movie S4. Optogenetic inhibition of the midbody B-type motor neurons in a wild-type worm resulted in whole-body paralysis. Note that all movies were played at 0.5× speed.

Movie S4

Movie S5. Optogenetic inhibition of the midbody B-type motor neurons in an *unc-9* mutant worm led to paralysis in the posterior region, whereas the anterior body undulation persisted. Note that all movies were played at 0.5× speed.

Movie S5

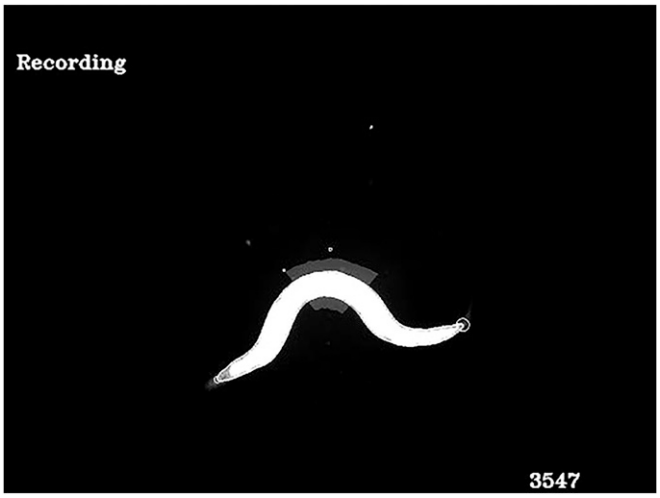

Movie S6. Overexpression of UNC-9 innexin in B-type motor neurons (P*acr-5*::UNC-9) caused whole-body paralysis. Worms were incapable of propagating body undulations along their bodies. Note that all movies were played at 0.5× speed.

Movie S6

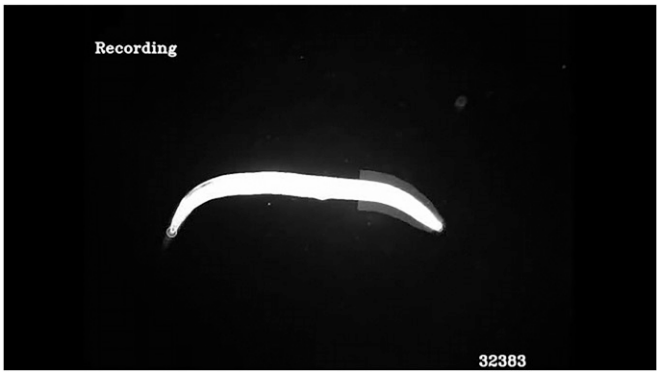

Movie S7. Optogenetic activation of AVB premotor interneurons (P*sra-11*::Chrimson) could trigger forward locomotion from the pause state. Note that all movies were played at 0.5× speed.

Movie S7

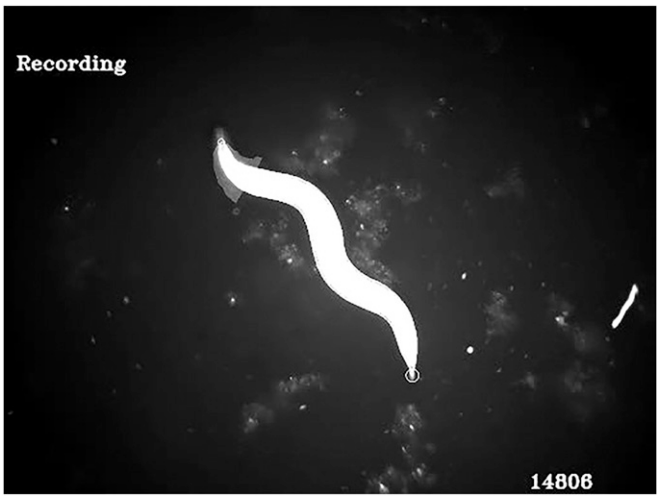

Movie S8. Optogenetic inhibition of AVB premotor interneurons (P*sra-11*::GtACR2) could abolish forward locomotion. Note that all movies were played at 0.5× speed.

Movie S8